FRET-based mesoporous organosilica nanoplatforms for in vitro and in vivo anticancer two-photon photodynamic therapy

Nicolas Bondon, Clément Charlot, Lamiaa Ali, Alexandre Barras, Nicolas Richy, Denis Durand, Yann Molard, Grégory Taupier, Erwan Oliviero, Magali Gary-Bobo, et al.

FRET-Based Mesoporous Organosilica Nanoplatforms for *In Vitro* and *In Vivo* Anticancer Two-Photon Photodynamic Therapy

Nicolas Bondon [a, b, *], Clément Charlot [a], Lamiaa M. A. Ali [c, d], Alexandre Barras [e], Nicolas Richy [b], Denis Durand [c], Yann Molard [b], Grégory Taupier [b], Erwan Oliviero [a], Magali Gary-Bobo [c], Frédéric Paul [b], Sabine Szunerits [e], Nadir Bettache [c], Jean-Olivier Durand [a], Christophe Nguyen [c], Rabah Boukherroub [e], Olivier Mongin [b, *] and Clarence Charnay [a, *]

[a] ICGM, University of Montpellier, UMR-CNRS 5253, 34293 Montpellier, France

[b] Univ Rennes, CNRS, ISCR (Institut des Sciences Chimiques de Rennes) - UMR 6226, ScanMAT – UAR 2025, F-35000, Rennes, France

[c] IBMM, University of Montpellier, UMR-CNRS 5247, 34293 Montpellier, France

[d] Department of Biochemistry, Medical Research Institute, Alexandria University, Alexandria, 21561, Egypt

[e] Univ. Lille, CNRS, Univ. Polytechnique Hauts-de-France, UMR 8520-IEMN, 59000 Lille, France

*Correspondence: nicolas.bondon@concordia.ca (N.B.); olivier.mongin@univ-rennes1.fr@umontpellier.fr (O.M.); clarence.charnay@umontpellier.fr (C.C.);

Tel.: +33-4-48-79-21-26 (C.C.)

ABSTRACT:

We report the synthesis of multifunctional periodic mesoporous organosilica nanoparticles (PMO NPs) with substantial two-photon absorption properties and targeting capability for two-photon excitation fluorescence (TPEF) and photodynamic therapy (TPE-PDT). Prepared using an adapted sol-gel synthesis, the nanoplatforms integrated two silylated chromophores in their three-dimensional matrix to maximize non-radiative Förster resonance energy transfer from a high two-photon absorption fluorophore donor to a porphyrin derivative, leading to an enhanced generation of reactive oxygen species. Various combinations of biodegradable and non-biodegradable bis(triethoxysilyl)alkoxysilanes were employed for the synthesis of the NPs, and the corresponding photophysical studies revealed high efficiency levels of FRET. Next, the cellular uptake and toxicities of pristine and functionalized NPs were evaluated on breast cancer cell lines upon TPEF and TPE-PDT. Notably, the use of TPE-PDT treatment led to high levels of phototoxicity on MCF-7 and MDA-MB-231 cancer cells with substantial effects when compared to one-photon excitation (OPE)-PDT treatment. Preliminary *in vivo* data on selective and biodegradable NPs showed a significant phototoxicity towards MDA-MB-231 on zebrafish xenograft embryos, making these advanced nanoplatforms promising candidates for future TPE-PDT-based cancer treatments.

A. INTRODUCTION

As the prevalence of cancer is not attenuated by currently available therapies, there is a rising need for more advanced strategies that can address today's shortcomings. Amongst them, two-photon excitation photodynamic therapy (TPE-PDT) is an emerging approach to treat a broad range of solid tumors and infection-associated diseases with three-dimensional spatial and temporal resolution and with increased penetration depth (> 2 cm) in living tissues. This provides a more suitable risk-benefit ratio for patients as compared to most renown one-photon excitation (OPE)-PDT that is also associated to lower spatial resolution and limited depth penetration.[1] Moreover, being able to excite above 700 nm, in the first transparency window, namely near-infrared I (NIR-I), is essential to prevent absorption of the light source by biological tissues and blood, minimizing laser absorption and scattering.[2] Presently, TPE-PDT can overcome this issue as excitation remains in the NIR spectral region.

FDA-approved organic dyes, such as methylene blue and indocyanine green, are not suitable for two-photon imaging and TPE-PDT due to their limited two-photon absorption (TPA) in the NIR, as well as their tendency to photobleach.[3] Recently, two-photon photosensitizers (PSs) with high capacity for simultaneous diagnosis via fluorescence imaging and therapy through photon energy conversion for generation of reactive oxygen species (ROS) have been reported to efficiently eradicate the targets, while minimizing side effects by diminishing the laser irradiation power.[4–6] However, efficient hyper-conjugated two-photon organic chromophores are generally limited by their poor biocompatibility and limited dispersion in biological media, which are detrimental features considering that they have poor selectivity for tumors in absence of specific functionalization.[7,8] Consequently, so-called "third generation" PS-based materials have been developed for TPE-PDT to provide solutions to the issues encountered with first- and second-generation PSs. So far, liposomes, dendrimers and nanoparticles (NPs) have been largely studied as biocompatible platforms where active elements (PSs, drugs, biomolecules, imaging agents, etc.) are entrapped inside, grafted onto their surface or even integrated within the platform scaffold during synthesis.[9–17] This advanced class of hybrid materials holds great promises for further improving PDT, thus, extending its potential in oncology, notably in combination with immunotherapy and radiotherapy.[18]

On the one hand, the integration of energy donor moieties with superior TPA capacity can also further increase ROS formation upon Förster Resonance Energy Transfer (FRET) to co-localized PS working as energy-accepting moieties.[19] In this respect, tetrapyrrole and porphyrin-based NPs are interesting candidates for biomedical imaging and therapeutic applications, owing to their high absorbance and strong fluorescence properties alongside with the advantages provided by their nanoscale size.[20] This approach offers the ability to design multifunctional NPs with competence for selective targeting and uptake, as well as for efficient biological tracking. Porphyrin-derived

chromophore units have been employed in a wide variety of NP synthesis, including particle coatings, reagents for carbon dot synthesis, as well as cross-linked or self-assembled NPs. This latter strategy can allow the formation of ordered porphyrin aggregates inducing cooperative enhancement effects, amplifying the absorption and ROS generation properties of the material.[21,22]

On the other hand, periodic mesoporous organosilica (PMO) NPs are noteworthy as versatile nanomaterials for biomedical applications.[23–32] With their hybrid structure, they can simultaneously integrate hydrophobic and hydrophilic fractions to build functional complex systems that can specifically reach the targeted cells or tissues. Moreover, fine mesopores can provide permeability to ROS diffusion from embedded PSs for PDT and are small enough to limit the release of cargos during transport.[14] Mesoporous organosilica nanostructures hold great potential for stimuli-triggered controlled delivery, such as by the action of pH,[33] temperature,[34] light,[35] or by redox reaction with glutathione reduced form (GSH), a natural tripeptide present in high rates in cancer cells.[36] In particular, this latter strategy can be employed to reduce the elimination time of sulfide-based biodegradable organosilica NPs when performing targeted PDT, hence, reducing the risks of long-term photosensitivity.

Combining these assets, the aim of this work consists in the design of two-photon responsive PMO NPs with enhanced performances for TPE-PDT resulting from efficient donor-acceptor FRET pairs. To achieve this goal, we proposed to directly integrate some highly-photoactive two-photon chromophores within PMO hybrid framework. Hence, a silylated three-branched organic fluorophore (F) - designed beforehand by our group -[37] possessing superior two-photon absorption cross section in the NIR-I region (*i.e.* > 200 GM between 700 and 850 nm) compared to commercially available organic dyes,[38] and the commercial 5,10,15,20-tetrakis(4-aminophenyl)porphyrin (P) were respectively chosen as donor and acceptor moieties. This porphyrin, after tetraethoxysilylation process, already demonstrated significant killing efficiency against MCF-7 cancer cells *in vitro* as an active two-photon PS integrated in the walls of PMO NPs.[39] For biological applications purpose, integrating these organic compounds in the framework of porous organosilica nanoparticles could also be beneficial to increase their bioavailability and stability in aqueous media.

The photophysical properties of the targeted PMO NPs were studied before and after covalent integration of F and P moieties in NPs. So far, different formulations of organoalkoxysilane precursors were tested, as well as surface functionalization, to prepare multifunctional materials with appropriate morphology, porosity and size, as well as stability and biodegradability features for biological applications. In particular, the PS used in this study already demonstrated ROS generation capability when integrated in various PMO frameworks, a feature mainly attributed to π-stacking effects of the PS molecules. Mezghrani and coworkers showed significant OPE-PDT and TPE-PDT effects of periodic mesoporous ionosilica NPs composed of P molecules towards MDA-MB-231 cancer cells with green

light illumination at 545 nm and two-photon red light illumination at 780 nm.[40–42] Aggad *et al.* observed slight TPE-PDT efficiency on MCF-7 cancer cells treated with ethylene-porphyrin PMO NPs upon 800 nm irradiation.[39] Based on these results, the therapeutic action of the presently targeted porphyrin-based PMO NPs were assessed on MCF-7 and MDA-MB-231 breast cancer cells lines. Their internalization in cancerous cells was monitored by two-photon excitation fluorescence using the intrinsic emissions of F and P chromophores, while the NPs toxicities upon PDT were studied using confocal microscopy. Ultimately, the phototoxicity of the functional NPs upon TPE-PDT were evaluated on xenografted zebrafish embryos.

B. RESULTS AND DISCUSSION

B.1 Design of multifunctional fluorophore-porphyrin-based PMO NPs

B.1.1 Preparation of sol-gel precursors

Prior to the sol-gel process leading to the formation of the desired organosilica NPs, the two selected chromophores were silylated by an addition process involving isocyanatopropyltriethoxysilane (ICPTES) in the presence of triethylamine. Thus, the porphyrin-derivative P was tetrasilylated, forming urea characteristic linkage (P-Si, **Figure 1**a). Silylation success of P-Si precursor was confirmed by ^{1}H NMR spectroscopy (**Figure S1**). After reaction of P with ICPTES, the formation of four urea units was revealed by the appearance of a signal at δ = 6.40 ppm (H_5, relative ^{1}H ≈ 4) designing the urea ^{1}H close to each silyl chain.
To reach the best FRET efficiency (Φ_{ET}), the spectral overlap between the emission spectrum of the energy donor (D) and the excitation spectrum of the energy acceptor (A) should be as high as possible. As demonstrated by fluorescence measurements (**Figure 1**b), F-Si/P-Si pair possesses a potential match between the large emission band of the fluorophore ($\lambda_{em.,\,max}$ = 548 nm) and porphyrin absorption bands (notably Q4 and Q3, respectively at 519 and 557 nm). Furthermore, fluorophore F-Si exhibits a high fluorescence quantum yield in the absence of energy acceptor, which is suitable for efficient energy transfer to porphyrin Q bands.

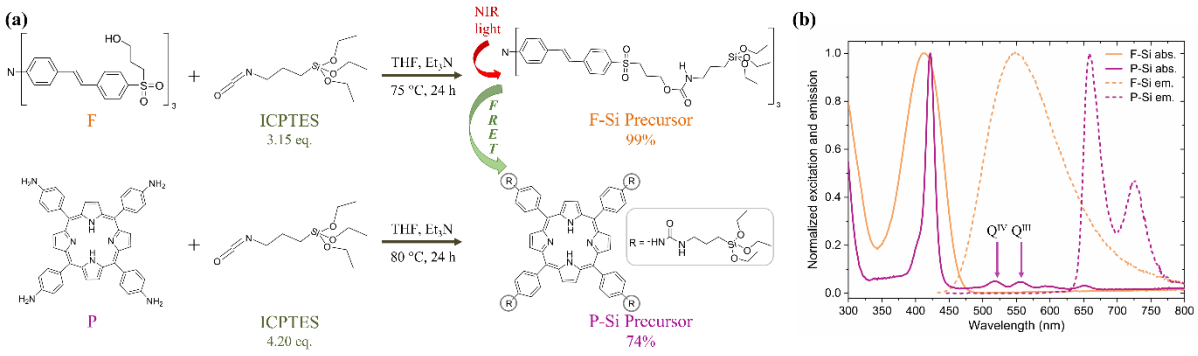

Figure 1. Two-photon chromophores preparation and Förster resonance energy transfer (FRET) strategy. (a) Silylation of two-photon chromophores for further use as precursors in sol-gel synthesis. Fluorophore F was trisilylated and porphyrin P was tetrasilylated with a slight excess of isocyanatopropyltriethoxysilane (ICPTES); (b) Normalized absorption and emission spectra of two-photon energy donor F-Si and two-photon energy acceptor P-Si. F-Si and P-Si were excited at their $\lambda_{abs., max.}$ determined by UV-visible spectroscopy in EtOH ($\lambda_{exc., F\text{-}Si}$ = 413 nm; $\lambda_{exc., P\text{-}Si}$ = 422 nm).

As the framework of the NPs is constituted of porphyrin J-aggregates, the absorption of porphyrin Q bands is red-shifted and is increased by a cooperative enhancement effect, thus, the use of F and P chromophores as a D/A pair for FRET-enhanced TPE-PDT is expected to result in higher production of ROS.[43–45]

B.1.2 Synthesis of fluorophore-porphyrin PMO NPs

Sol-gel synthesis of PMO NPs is generally performed in the presence of surfactant micelles around which nuclei grow to build porous NPs with well-defined texture and morphology. In our study, the synthesis was based on a modified Stöber process with CTAB cationic surfactant as a template. The reaction was performed in basic conditions using sodium hydroxide to ensure a better control of the reaction kinetics, thus, a better control of the NPs' sizes. For this study, four types of fluorophore-porphyrin (F-P) mesoporous organosilica NPs were synthesized. Three symmetrical organoalkoxysilane precursors, with generic chemical formula $(EtO)_3$-Si-R-Si-$(OEt)_3$, were used in four different combinations along with a small portion of two-photon silylated chromophores (**Figure 2**). It is important to have in mind that the organic bridging group of each precursor can drastically influence pore diameter, pore volume, as well as NPs morphology and size.[46] Thus, experimentations were focused on the use of 1,2-bis(triethoxysilyl)ethane (E) or 1,2-bis(triethoxysilyl)ethene (ENE) as the major precursor, which present low steric hindrance effects compared to F-Si and P-Si chromophores. E and ENE precursors can provide long-range ordering of the formed mesoporous structure as well as higher specific surface areas.[46] In addition to that, two of the four types of NPs were synthesized by mixing either E or ENE with bis[3-(triethoxysilyl)propyl]tetrasulfide (4S) in a molar ratio of 80:20. This precursor owns easily breakable S-S bonds, which are known to confer biodegradability properties to the NPs.[25,36,47]

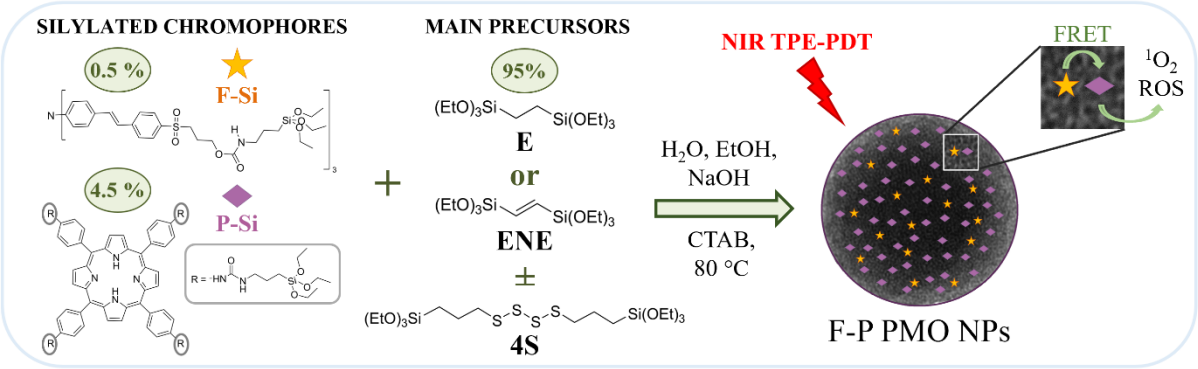

Figure 2. Synthesis conditions of fluorophore-porphyrin (F-P) PMO NPs. In the case of ethylene (ENE)-based NPs, racemic β-citronellol was used as a co-structure-directing agent.

After optimization of the synthetic conditions, one experimental protocol was established for E-based syntheses (E-F-P and E-4S-F-P) and another one was chosen for ENE-based syntheses (ENE-F-P and ENE-4S-F-P). Both processes were performed in mild conditions at 80 °C. For the preparation of ENE-based NPs, racemic β-citronellol was co-added with CTAB as a co-structure-directing agent to provide better control over NPs morphologies and pore features *via* the decrease of micellar surface free energy.[48,49] Due to the reduced dispersion of F-Si and P-Si in water, all the precursors were premixed in a small aliquot of absolute ethanol with a 1:0.045:0.005 constant molar ratio (main precursors:P-Si:F-Si), right before addition in the sol-gel medium, while maintaining the stability of nuclei formation (**Table S1**).

Transmission electron microscopy (TEM) imaging revealed the formation of polydisperse nanospheres with well-defined small mesoporosity (**Figure 3**b) for E-F-P, E-4S-F-P, ENE-F-P and ENE-4S-F-P PMO NPs, with respectively 142 ± 48 nm, 163 ± 75 nm, 153 ± 61 nm, and 158 ± 60 nm average particle sizes (**Figure 3**a**, Table 1**). Compared to similar PMO synthetic procedures using combinations of E, ENE and 4S precursors only, the integration of small fractions of silylated chromophores caused significant changes on NPs structure, morphology, and texture of the obtained NPs. In particular, ENE PMO NPs without additional chromophore-based precursor have been reported to display a worm-like shape.[50] Thus, the averaged hydrodynamic diameters of E-F-P, E-4S-F-P, ENE-F-P and ENE-4S-F-P PMO NPs, determined by dynamic light scattering (DLS) measurements, were respectively 492 ± 8 nm, 388 ± 5 nm, 524 ± 18 nm and 616 ± 11 nm, and these overestimate diameters resulted in the size polydispersity. Indeed, the light scattering processing is based on an algorithm that takes the Rayleigh law into account, thus, nanoparticles with large hydrodynamic size are diffusing much more than small ones, which balances the average size.

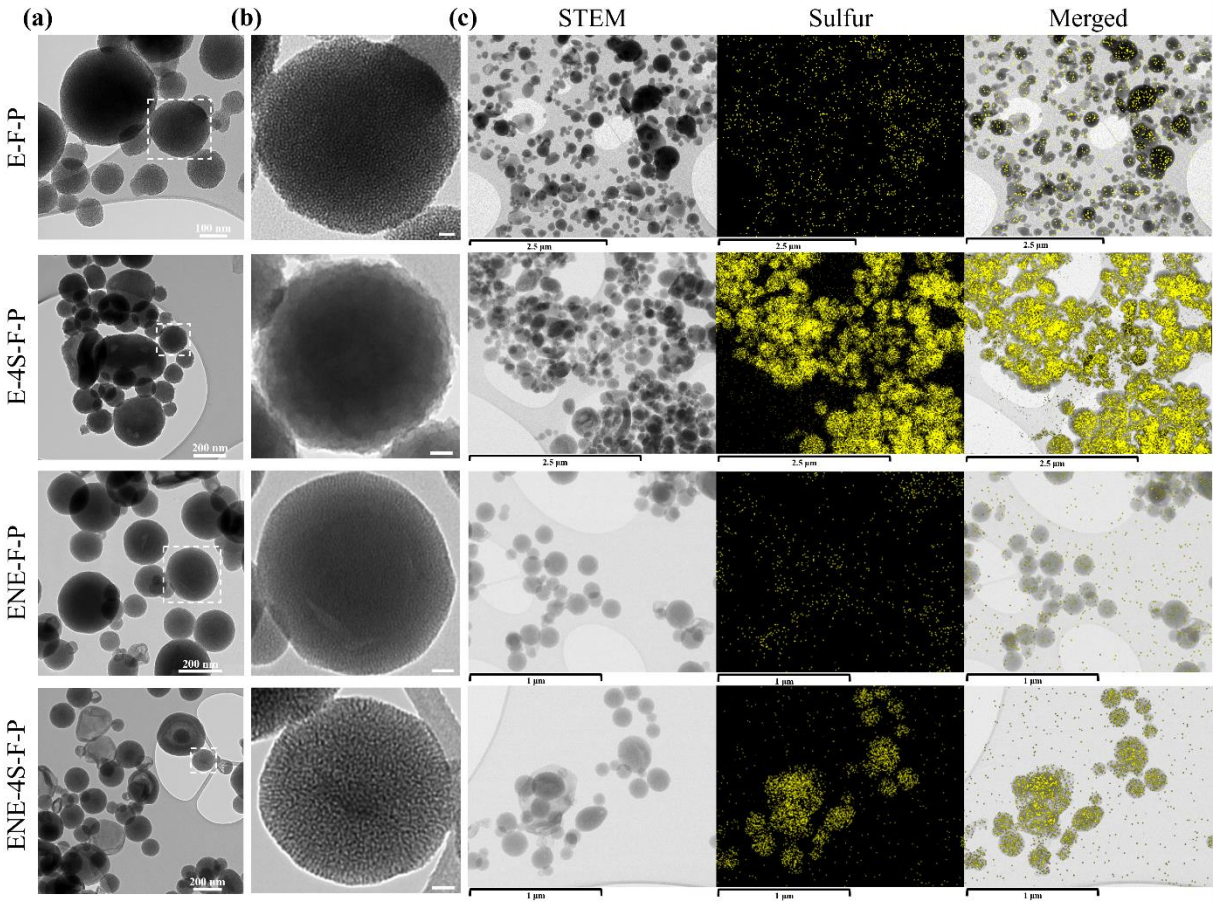

Figure 3. Morphological and structural characterization of F-P PMO NPs. (a) TEM images. Scale bars: 100 nm (E-F-P); 200 nm (others). (b) High magnification depicting NPs mesoporosity. Sclae bars: 20 nm (c) STEM-EDX mapping of F-P PMO NPs. Merged images reveal the presence of S in the different NPs. Scale bars: 2.5 µm (E-F-P and E-4S-F-P); 1.0 µm (ENE-F-P and ENE-4S-F-P).

The textural properties of the formed NPs (*i.e.*, specific surface area (SSA), pore diameter and pore volume) were screened by nitrogen sorption measurements on samples previously degassed under reduced pressure. N_2 adsorption-desorption isotherm curves revealed type-IV profile with a step from 0.3 to 0.5 P/P_0, characteristic of a mesoporous structure (**Figure S2**). Moreover, the regular distance between adsorption and desorption branches at $P/P_0 > 0.5$ (type H1 hysteresis) is indicative of a narrow mesopore size distribution.[51] As calculated by Barrett–Joyner–Halenda theory, E-based and ENE-based PMO NPs were mainly composed of 2.7 nm-wide pores. When introducing 4S, the nanostructures present an increased portion of 3.8 nm-wide pores. Overall, these differences reflect the impact of mixing precursors with various organic moieties.

In addition, high specific surface areas (SSAs) were calculated from Brunauer-Emmett-Teller method,[52] ranging from 500 to 875 $m^2 g^{-1}$. All as-synthesized NPs present negative zeta potential values, which is attributed to the prevalence of silanolate functions on their surface (**Table 1**).

Table 1. Main characterization data of E-F-P and ENE-F-P PMO NPs. [a] z average hydrodynamic diameter in ethanol, n = 3 independent experiments. [b] Average diameters of n ≥ 100 counts determined on TEM images. [c] Zeta potential measurement, n = 3 independent experiments (0.25 mM PBS). [d, e, f] SSA: Specific Surface Area, d_p: pore diameter, V_p: pore volume. SSA was calculated by Brunauer-Emmett-Teller method; pore diameters (most/lowest abundant) and volumes were obtained from the desorption branch of nitrogen sorption isotherm curves and calculated by Barrett–Joyner–Halenda theory with only mesopores (1.7-60 nm) taken into consideration.

Pristine PMO NPs	**DLS[a] (nm)**	**PDI**	**TEM[b] (nm)**	**ζ[c] (mV)**	**SSA[c] (m^2 g^{-1})**	**d_p[d] (nm)**	**V_p[e] (cm^3 g^{-1})**
E-F-P	492 ± 8	0.34 ± 0.06	142 ± 48	-23.7 ± 0.7	875	2.7/3.8	0.66
E-4S-F-P	388 ± 5	0.24 ± 0.02	163 ± 75	-38.2 ± 1.5	500	3.8	0.64
ENE-F-P	524 ± 18	0.30 ± 0.10	153 ± 61	-34.4 ± 1.0	856	2.7/3.8	0.74
ENE-4S-F-P	616 ± 11	0.30 ± 0.03	158 ± 60	-44.7 ± 0.4	699	3.8	0.66

As the sulfonate groups in fluorophore F are the only source of sulfur atoms amongst the sol-gel precursors, STEM-EDX mapping was performed to assess its presence in the structure of NPs, revealing little concentrations of sulphur atoms in both E-F-P and ENE-F-P PMO NPs. For E-4S-F-P and ENE-4S-F-P PMO NPs, a much higher sulphur content attributed to the bispropyltetrasulfide moieties was observed (**Figure 3**c). Similarly, the integration of F, P and sulphur-based moieties was further confirmed by ^{13}C NMR studies (**Figure S3**). In addition, degradation studies of 4S-based NPs were performed upon simulation of an environment rich in reduced GSH to produce tetrasulfide bond cleavage. The tested GSH concentration (10 mM) is representative of the cytosol environment of cancer cells, which is known to be several times superior to GSH concentration in healthy cells.[53] TEM images revealed substantial fragmentation of E-4S-F-P PMO NPs after several days in the presence of mercaptoethanol (GSH-equivalent), while the structure of NPs remained intact in absence of the reducing agent (**Figure S4**).

Altogether, these studies demonstrate the great structural ordering of the newly synthesized fluorophore-porphyrin PMO NPs. With their colloidal stability, high surface area and well-defined porosities, these NPs could be suitable platforms facilitating intraparticle and interparticle ROS dynamics, as well as within defined biologically-relevant environments.

B.1.3 Functionalization strategy for biological targeting

Functionalization of NPs with a mannose phenyl squarate derivative (MAN, prepared in our lab) was chosen to improve selectivity towards lectins that are overexpressed at the surface of cancer cells, with the aim to increase NPs cellular uptake and PDT efficiency.[54,55]

The main issue associated with organosilica NPs is the adhesion of proteins and blood platelets to their surface. Attachment of hydrophilic PEG grafts onto F-P PMO NPs surface is conventionally used to render them less sensitive to recognition by the immune system.[56,57] In fact, PEG inhibits non-specific and specific protein interaction, aiming to reduce the reaction of macrophages and other immune cells, thus increasing the circulatory half-life of the functional NPs.[58]

Hence, a 25:1 (mol:mol) ratio between PEG-Si and 11-aminoundecyltriethoxysilane (AUTES) was added during synthesis to the growing PMO NPs (**Figure 4**). Then, the (PEG-Si/AUTES)-grafted NPs, named as F-P PMO@PEG, were further modified by post-grafting reaction between AUTES primary amines and MAN ether groups to obtain MAN-grafted NPs, named as F-P PMO@MAN.

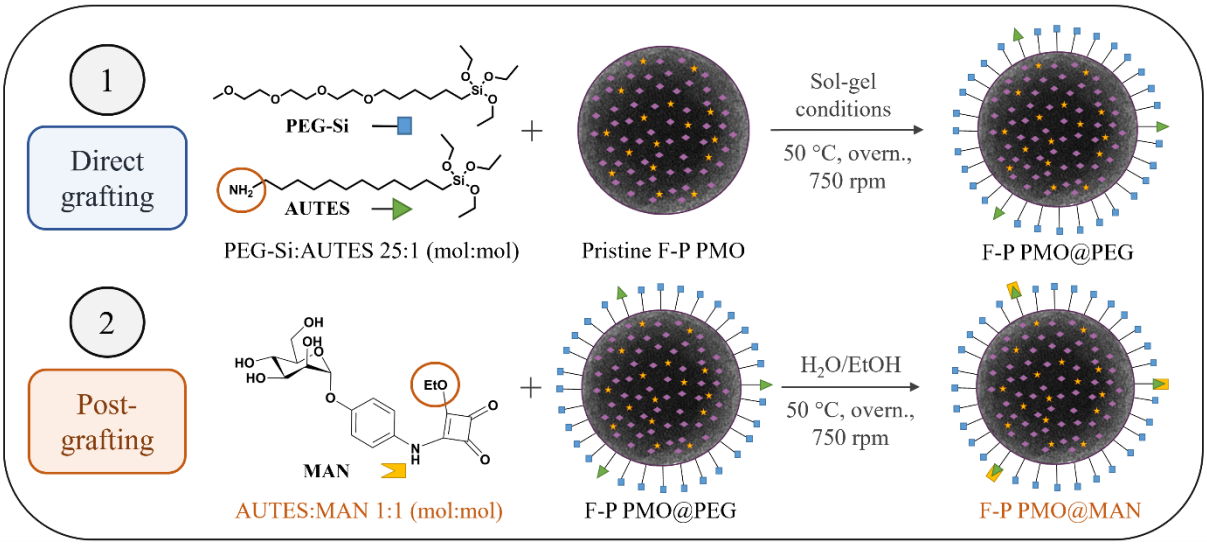

Figure 4. Functionalization conditions of F-P PMO NPs. A PEG-Si:AUTES mixture and MAN were introduced in two separated steps with a 1:0.220:0.009:0.009 (mol:mol) relative theoretical ratio compared to the initial composition of sol-gel precursors.

AUTES grafting efficiency was evaluated with fluorescamine (FA), a commercially available fluorescent probe routinely used for the detection of primary amines and the analysis of amino acid and proteins for biochemistry applications.[59] Such reaction of AUTES primary amine with FA produces a chromophore with high fluorescence (**Figure S5a**), allowing to perform amine titration after a fluorescence-intensity scaling procedure using a range of standards at various concentrations. This technique is particularly suited for the quantification of the low AUTES content introduced in the reaction mixture, as it enables detection down to the picomolar level.[60] Four standard samples of pyrrolinone derivative, formed by FA:AUTES 1:1 (v:v) mixtures, were thus analysed by fluorescence

spectroscopy and showed a linear behavior, as revealed by the significant value obtained for the square of the linear correlation coefficient, *i.e.*, $R^2 > 0.99$ (**Figure S5c**).

Homogeneous AUTES grafting concentrations were calculated from measured pyrrolinone fluorescence intensities at $\lambda_{em.}$ = 482 nm, with values between 6.0 and 8.1 µmol *per* milligram for the four types of NPs (**Figure S5d**). Next, in order to accomplish a full MAN grafting on the surface-pending amine functions, the necessary amount to substitute all of them (*i.e.*, 1:1 (mol:mol)) was estimated for each sample with respect to PEG-grafted NPs (formula in **Experimental Section**).

B.2 Photophysical studies

B.2.1 Comparison of NPs and chromophore precursors

Alongside structural characterization of the chromophore-based NPs, their photophysical properties were studied to confirm the integration of F-Si and P-Si chromophores within the framework of the NPs during sol-gel synthesis. The resulting organosilica NPs display a broad fluorescence emission band upon single-photon excitation at 413 nm in EtOH, with a maximum at 544 nm, which is in line with F-Si fluorescence profile with a maximum emission at 548 nm (**Figure S6a**). Compared to the silylated porphyrin, a small bathochromic shift and a broadening of the two porphyrin emission bands were observed for F-P PMO NPs due to the formation of J-aggregates and π-stacking of the macrocycles within PMO frameworks. In addition, lower fluorescence emission intensities were observed from F moieties (440-625 nm) compared to P moieties (625-800 nm). This observation is in accordance with the optimized 9:1 (mol:mol) ratio determined by *ab initio* calculations between P-Si and F-Si precursors to maximize energy transfer efficiency and PDT outcome.[61,62]

B.2.2 FRET studies in chromophore-based NPs

To go further and evaluate FRET efficiency from F energy donors (D) to P energy acceptors (A), a quantification method was established by comparison of F-P PMO NPs fluorescence emission properties with similar NPs prepared with only fluorophore F (denoted as D) or with only porphyrin P (denoted as A). Energy transfer from F to P moieties was assessed by comparing the emission profiles of F PMO (D), P PMO (A) and F-P PMO (D-A) NPs (**Figure 5**) measured at the same mass concentration in EtOH (*i.e.*, 44 µg mL^{-1}). As F-Si and P-Si molar ratios are kept constant in all studied PMO materials, the number of absorbed photons by F is also the same, which is mandatory to properly compare I_D and $I_{D\text{-}A}$ fluorescence intensities. Furthermore, P PMO NPs are not emissive in F emission range (440-625 nm). Consequently, the decrease of F fluorescence can be studied to assess FRET efficiency (Φ_{ET}).

Hence, each family of chromophore-based PMO NPs was subjected to OPE (**Figure S6b** to **e**) and TPE, and FRET efficiency was calculated accordingly. NPs suspensions were irradiated at 413 nm in the case of one-photon studies, which corresponds to the maximum absorbance wavelength of fluorophore F, while in two-photon studies, an excitation wavelength of 850 nm was used, thus, close to twice the

OPE wavelength. A higher wavelength was chosen because, in these conditions, the two-photon absorption of P is very low, while F moieties are still displaying a high two-photon absorption cross-section (205 GM).[37] In addition, an excitation at a lower wavelength would require a filter which would cut most of P emission, whereas, in this study, the use of a 750 nm-filter upon TPE at 850 nm afforded a quasi-full emission spectrum in the visible region.

In the case of E-based PMO NPs (**Figure 5**a and **5**b), the decrease of donor fluorescence intensity in between F PMO and F-P PMO NPs at 544 nm or in the 440-625 nm range leads in both cases to 93% and 84% FRET efficiencies, respectively, for E-F-P and E-4S-F-P PMO NPs.

The shape of the residual emission band of the donor remains unchanged in E-F-P PMO NPs in comparison with that of E-F PMO NPs, which confirms that a non-radiative energy transfer mechanism (*i.e.*, FRET) is involved. A radiative transfer mechanism (so-called *trivial* transfer) would have led to a decrease of the fluorescence intensity only in the regions of the spectral overlap, which is not the case here.[63]

It is also observed that the fluorescence intensity of the energy acceptor increases in the presence of the energy donor in the 650-750 nm range, but this effect is limited because a consequent part of the transferred energy serves to boost ROS production of P moieties.

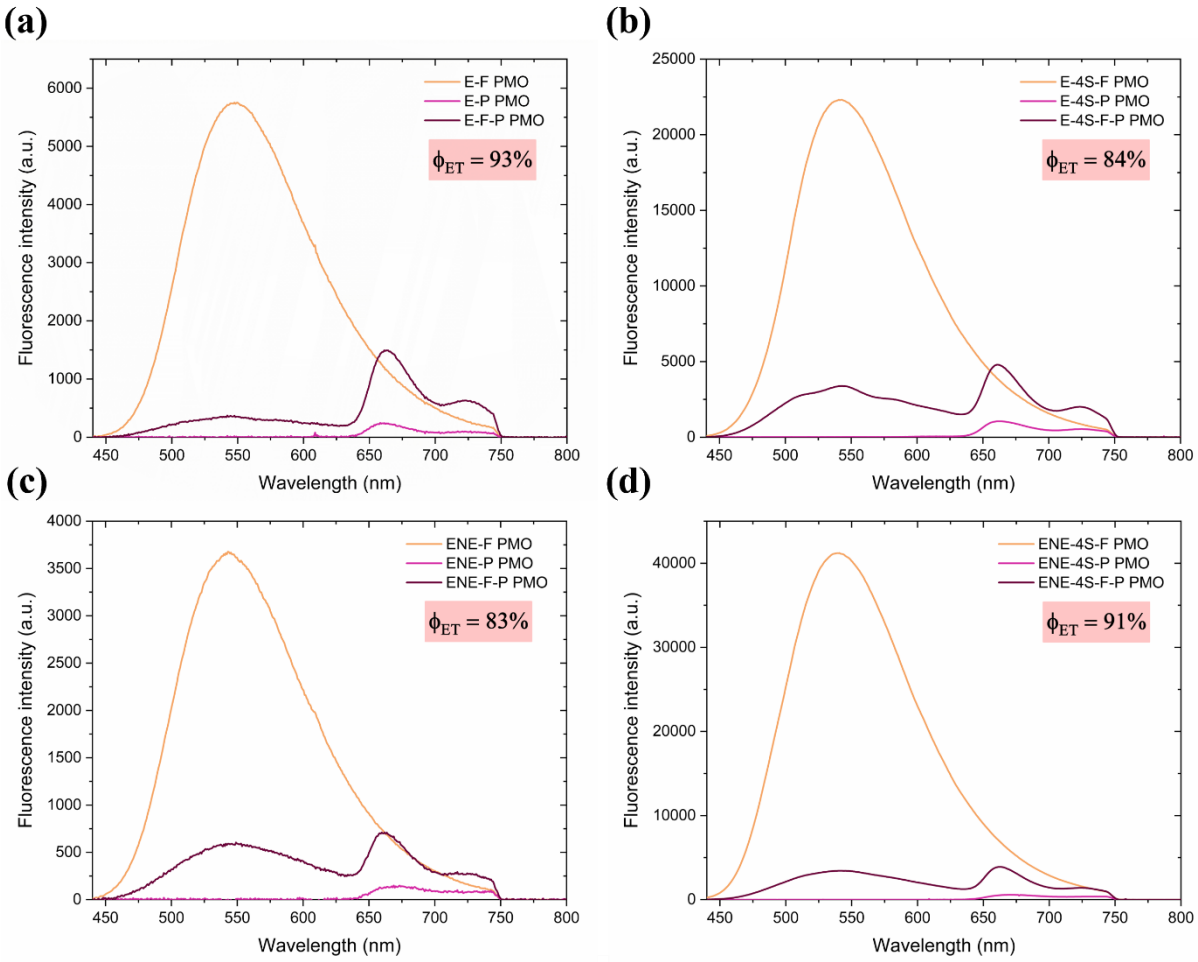

Figure 5. Fluorescence emission spectra of chromophore-based PMO NPs upon two-photon irradiation and associated FRET efficiencies. Energy donor-based (F PMO), energy acceptor-based (P PMO) and associated donor-acceptor-based (F-P PMO) NPs emission profiles were compared upon two-photon irradiation. (a) E PMO NPs. (b) E-4S PMO NPs. (c) ENE PMO NPs. (d) ENE-4S PMO NPs. F fluorescence is quenched by P *via* energy transfer, and P emission is increased.

Similarly, the potential for efficient energy transfer from F to P was studied in ENE-based PMO NPs. Qualitatively, porphyrin seems to be less fluorescent (650-800 nm range) for these NPs. The partial quenching of donor F allowed estimating FRET efficiency of 83% and 91%, respectively for ENE-F-P and ENE-4S-F-P PMO NPs (**Figure 5**c and **5**d). This diminution is accompanied by concomitant increase of P fluorescence.

Two-photon FRET efficiencies were very similar to one-photon efficiencies (as reported in **Figure S6**) which is supporting that all NPs undergo FRET mechanisms. As high Φ_{ET} values were deducted from the comparison of the donor emission between F PMO NPs and F-P PMO NPs, these nanosystems are expected to be beneficial for PDT of cancers, thus, anticancer evaluation of PDT efficiency was envisaged.

B.3 *In vitro* therapeutic potential

Anticancer studies were performed *in vitro* upon photodynamic excitation. Pristine, PEG-grafted and MAN-grafted samples of each F-P PMO NPs were compared. Firstly, photodynamic activities were evaluated upon OPE at a wavelength of 525 nm, where fluorophore absorption does not overlap with the Q^{IV} bands of porphyrin (**Figures 1**, **S6** and **S7**). The porphyrin is directly excited with its Q^{IV} band. In this case, cell viability was determined by using MTT chromophore to estimate cells survival rates. For those experiments, the negative control was associated with cancer cell viability in the absence of NPs. OPE-PDT results for irradiation times of 10 min are presented in **Figure 6** for MAN-grafted NPs and in **Figure S8** for pristine and PEG-grafted NPs. In dark conditions, the viability of MCF-7 cancer cells was always satisfying at 50 µg mL^{-1}, showing the low cytotoxic effect of all NPs. After OPE treatment, ENE-4S-F-P PMO NPs samples caused either unsignificant or low reductions in viability (**Figure 6** and **Figure S8**). Conversely, irradiation in the presence of MAN-grafted NPs caused 59%, 44% and 25% cell death, respectively for E-F-P@MAN, E-4S-F-P@MAN and ENE-F-P@MAN PMO NPs (**Figure 6**).

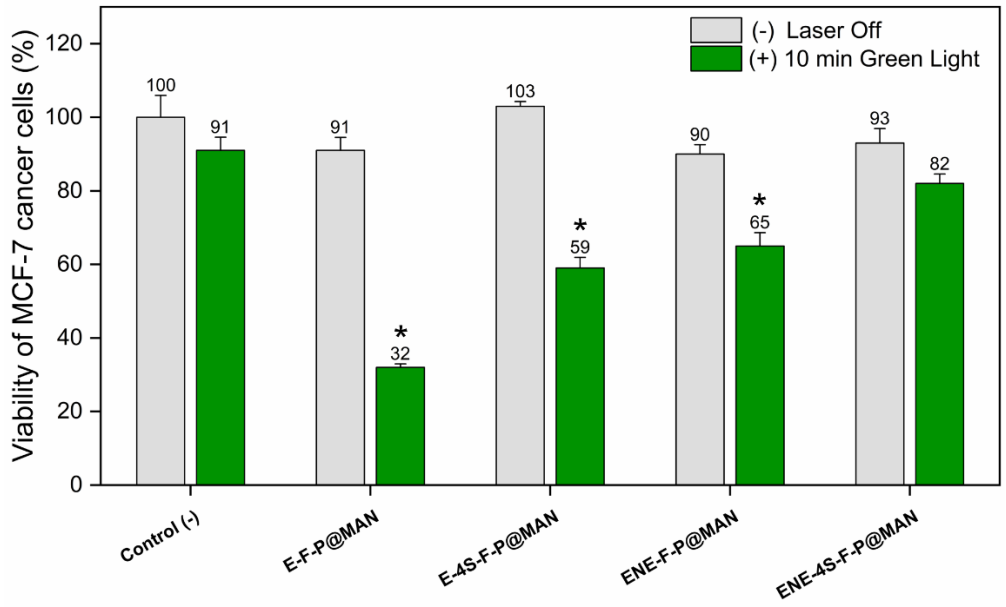

Figure 6. One-photon excitation (OPE)-PDT assays using F-P@MAN NPs. OPE-triggered MCF-7 cancer cells killing after incubation with NPs at 50 µg mL^{-1} for 24 h and irradiation at 525 nm for 10 min (34 J cm^{-2}). Lines represent standard deviations of three independent experiments. Differences between irradiated and non-irradiated samples were considered statistically significant when p values were less than 0.05 (*p <0.05).

Before assessment of the therapeutic potential of TPE-PDT, confocal light scanning microscopy of living breast cancer MCF-7 cells treated with 50 µg mL^{-1} of F-P PMO NPs for 24 h was performed. After 780 nm TPE, the NPs generated high fluorescence intensities in the biological medium and high levels of cell internalization (**Figures 7**a, **S9a** and **S10**). This demonstrates the bio-imaging potential of

these nanomaterials upon TPE in the NIR-I region independently of the PMO framework in which the chromophores are integrated.

Then, considering the advantageous two-photon properties of the chromophore-based PMO NPs, TPE-PDT studies were performed *in vitro* at 780 nm to preferentially irradiate fluorophore moieties for optimal FRET efficiency. Thus, living cells nuclei were stained using Cell Mask ™ Orange Plasma Membrane and counted on an EVOS™ M5000 imaging system after optimization of photograph parameters (brightness, gain, exposure) to properly distinguish NPs and cellular fragments from living MCF-7 cancer cells.

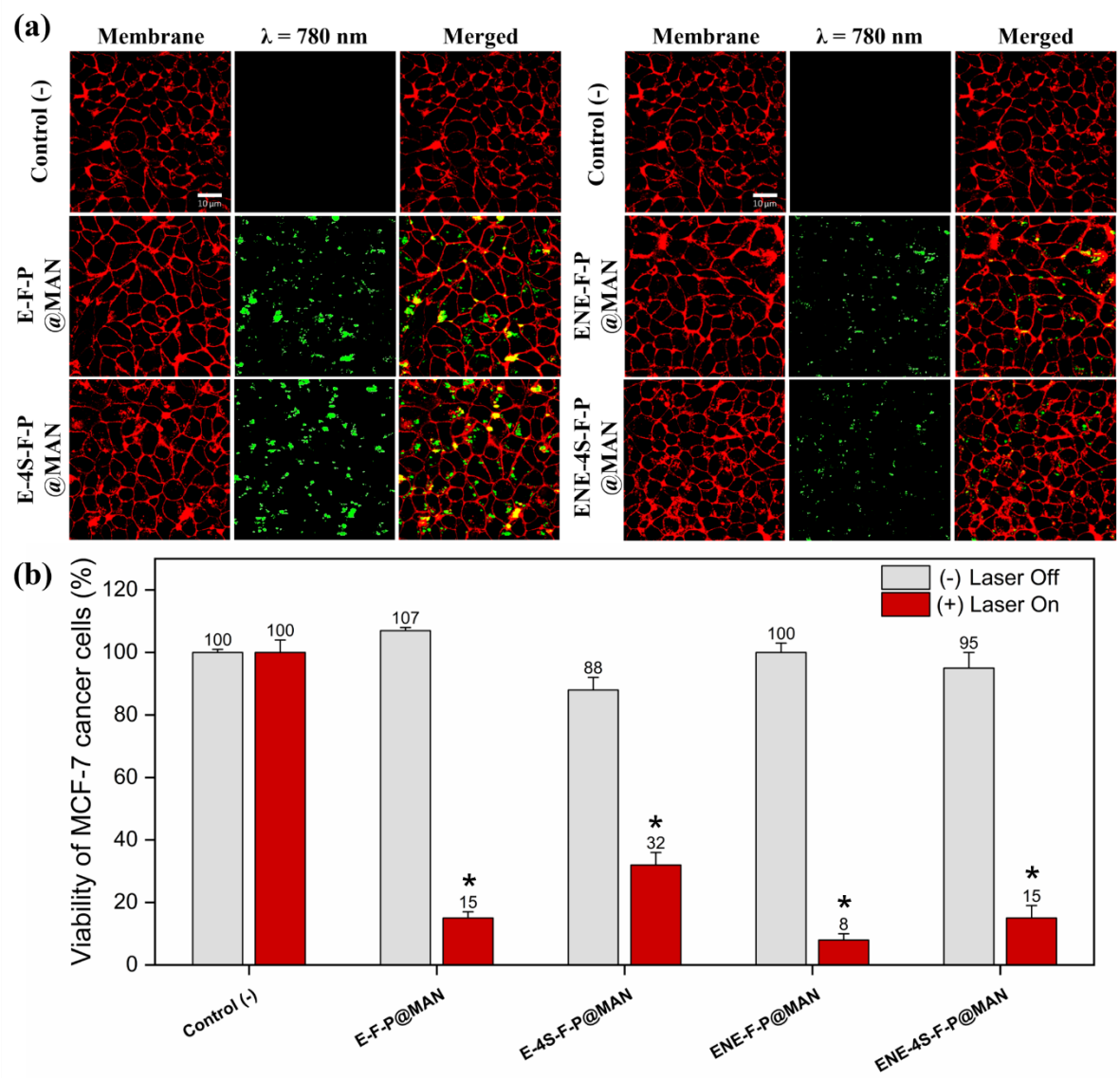

Figure 7. Cell internalization and anticancer TPE-PDT assays using F-P@MAN NPs. (a) Cell internalization study of MAN-grafted F-P PMO NPs at 50 µg mL^{-1} using confocal microscopy imaging. After incubation for 24 h, MCF-7 cancer cells were stained with Cell Mask™ Orange Plasma Membrane and then visualized at 561 nm (membrane) and 780 nm (F-P PMO NPs). Images were obtained with Carl Zeiss LSM780 confocal fluorescence microscope using a high magnification (63×/1.4 OIL Plan-Apo). (b) TPE-triggered MCF-7 cancer cells killing after incubation with NPs at 50 µg mL^{-1} for 24 h and irradiation at 780 nm (3 × 1.26 s). Lines represent standard deviations of six or eight independent experiments. Differences between irradiated and non-irradiated samples were considered statistically significant when p values were less than 0.05 (*p <0.05).

Contrary to OPE-PDT assays, TPE-PDT in the NIR induced high levels of toxicity with 56 to 96% cancer cell death for all F-P PMO NPs at 50 µg mL^{-1}, independently of the functionalization strategy (**Figure 7**b and **Figure S8**). This result originates from the great optical properties of F and P chromophores at two-photon, and from the crossing by specific electronic excited states due to different selection rules during TPE. Altogether, the discrepancy in between one-photon and two-photon PDT efficiency suggests that the pair of chromophores is suitable for a two-photon-based strategy, providing FRET-enhanced killing efficiency of cancer cells.

B.4 Therapeutic activity on xenografted zebrafish embryos

The promising *in vitro* TPE-PDT results performed on MCF-7 cells encouraged us to test the effectiveness of F-P NPs *in vivo*. For that, ENE-4S-F-P NPs were chosen for their biodegradability properties as well as their superior killing efficiency compared to E-4S-F-P NPs counterparts, with respectively 80 to 90% and 42 to 56% reduction in viability after irradiation, depending on the surface composition (**Figure 7**b for MAN-grafted and **Figure S8** for others). Zebrafish model was chosen for this study because it is considered as a substitutive animal model for small mammals and showed several advantages including the transparency.[64] In fact, the induction of xenograft in Casper zebrafish embryos using MCF-7 cells was not possible due to the aggregations, which block the needle of microinjection. Therefore, MDA-MB-231 breast cancer cells were used as they were well separated and form less aggregates.

The toxicity of ENE-4S-F-P NPs was beforehand studied *in vitro* on MDA-MB-231 cancer cells, demonstrating no dark cytotoxicity up to 50 µg mL^{-1} (**Figure S11**). Alongside electron spin resonance assays that confirmed the generation of ROS (**Figure S12**), ENE 4S-F-P@PEG and ENE-4S-F-P@MAN were effective at killing cells after 5 h of incubation, suggesting that they are well internalized (**Figure S13a**). Extending the incubation time (20 h) seems to enable ENE 4S-F-P@PEG to increase its internalization and therefore its efficacy (20% viability after PDT instead of 43%), whereas for ENE-4S-F-P@MAN NPs with mannose receptor targeting elements, the PDT efficiency seems already maximal after 5 h incubation time with only 15% and 17% of viability after 5 and 20 h, respectively (**Figure S13b**). In addition, TPEF studies revealed that the intrinsic fluorescence of ENE-4S-P and ENE-4S-F-P NPs was strong enough to visualize their cellular internalization. This way, the fluorescence emission of either F or P can be used to track the NPs, while avoiding an overlap in fluorescence emission wavelength with common cell stains (**Figure S14**). These data suggest that targeting elements on NPs enables faster and more specific internalization of NPs, thus enhancing therapeutic and diagnostic applications.

Thus, MDA-MB-231 breast cancer cells expressing the RFP protein were used for the induction of xenografts. Cells previously treated (or not) with ENE-4S-F-P@MAN NPs were injected in the yolk of 30 hpf embryos (**Figure 8**a). Twenty-four hours after cell injection, embryos were imaged, then

exposed to 780 nm irradiation followed by imaging 24 h later. The xenograft growth was monitored by quantifying the fluorescence intensity of the xenograft before and after irradiation (**Figure 8**b). Results showed no effect of the irradiation conditions on embryos with non-treated cell xenograft (control), the xenograft fluorescence % values were 158 ± 11% and 144 ± 16% for control embryos group non-exposed and exposed to irradiation, respectively.

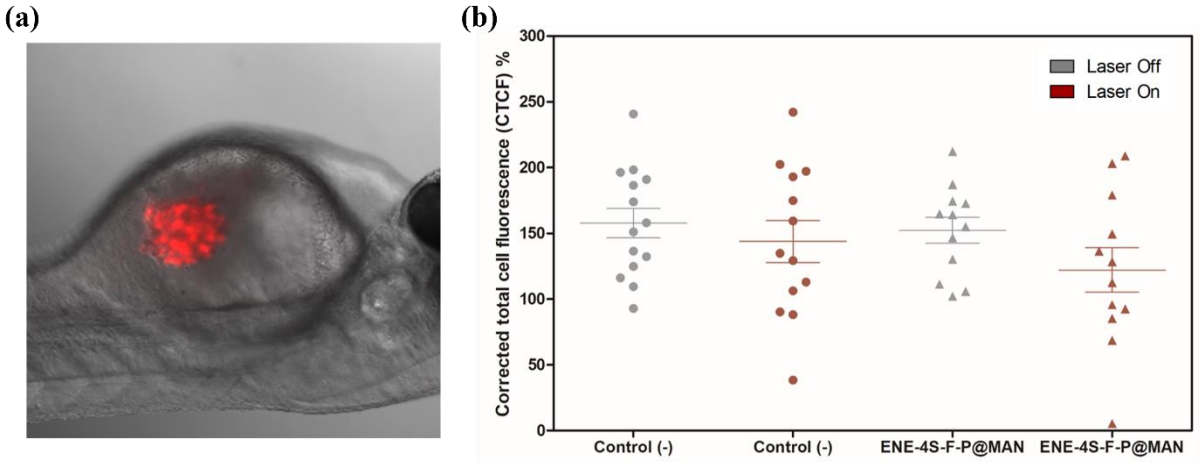

Figure 8. TPE-PDT assays on zebrafish embryos xenografts using CTCF assay. (a) Representative image of 48 hours post-fertilization of Casper embryo with human breast cancer (MDA-MB-231-Luc-RFP) cells xenograft fluorescent in red. (b) Quantification of xenograft fluorescence percentage for each embryo at 24 h after 780 nm irradiation (6 × 1.26 s) of Casper Zebrafish xenografted with MDA-MB-231-Luc-RFP cancer cells preincubated (or not) with ENE-4S-F-P@MAN. The Total Cell Fluorescence (CTCF) % was calculated as CTCF after irradiation/ CTCF before irradiation*100. Each point represents an embryo. Data are presented as mean ± SEM.

However, when the embryos with ENE-4S-F-P@MAN NPs-treated cell xenograft (ENE-4S-F-P@MAN) were exposed to irradiation, the xenograft fluorescence % was decreased. Values were 152 ± 10% and 122 ± 17% for ENE-4S-F-P@MAN embryos group non-exposed and exposed to irradiation, respectively. These results showed the promising TPE-PDT effect of ENE-4S-F-P@MAN.

C. MATERIALS AND METHODS

C.1 Chemicals and Materials

Unless otherwise specified, ACS reagent grade starting materials and solvents were used as-received from commercial suppliers without further purification.

Deionized water (resistivity = 18.2 MΩ.cm) obtained from an Aquadem™ system (Veolia Water Technologies, Saint-Maurice, France) was used for cancer cell-related experiments. ASTM type I ultrapure water (resistivity = 18.2 MΩ.cm) from an Elga PURELAB® Flex purification system (Veolia Water Technologies, Saint-Maurice, France) was used in all other experiments. Tris{4-[(1E)-2-{4-[(3-hydroxypropyl)sulfonyl]phenyl}ethenyl]phenyl}amine (F) and tris{4-[(1E)-2-{4-[(3-{*N*-[3-(triethoxysilyl)propyl]carbamoyl}propyl)sulfonyl]phenyl}ethenyl]phenyl}amine (F-Si) were synthesized according to our previously reported protocol.[37] p-[*N*-(2-Ethoxy-3,4-dioxocyclobut-1-

enyl)amino]phenyl-α-D-mannopyranoside (MAN) was synthesized following Sperling *et al.*'s protocol.[65] 1,2-Bis(triethoxysilyl)ethane (E, 96%), bis[3-(triethoxysilyl)propyl]tetrasulfide (4S, ≥ 90%), 3-(isocyanatopropyl)triethoxysilane (ICPTES, 95%), cetyltrimethylammonium bromide (CTAB, > 98%), sodium hydroxide pellets (NaOH, ≥ 98%), ammonium nitrate (NH_4NO_3, > 98%), phosphate buffer solution (PBS, 1X, 100 mM, pH 7.4), (2,2,6,6-tetramethylpiperidin-1-yl)oxyl (TEMPO ,98%), 2-mercaptoethanol (ME, > 99%), ethyl acetate, hexane (≥ 97%), dimethylsulfoxide-d_6 (99.9 atom% D), Whatman® qualitative filter paper, Grade 6 (3 µm) and Fluoropore® PTFE membrane filters (0.22 µm) were purchased from Merck (Saint-Quentin-Fallavier, France). β-Citronellol (95%), fluorescamine, dimethylsulfoxide (DMSO, 99.7 %), hydrochloric acid (HCl, ≥ 37%), methanol (≥ 99.9%), tetrahydrofuran (THF, 99.5 %, extra dry over molecular sieves), boric acid and triethylamine (Et_3N, > 99%) were purchased from Thermo Fisher Scientific (Illkirch-Graffenstaden, France). 1,2-Bis(triethoxysilyl)ethylene (ENE, 95%, 80% trans-isomer) was obtained from abcr GmbH (Karlsruhe, Germany). Ammonia (28%), absolute ethanol (EtOH) and ethanol (96%) were obtained from Carlo Erba Reagents (Cornaredo, MI, Italy). 5,10,15,20-Tetrakis(4-aminophenyl)porphyrin (P, ≥ 98%) was obtained from PorphyChem (Dijon, France). (6-{2-[2-(2-Methoxy-ethoxy) ethoxy]ethoxy}hexyl)triethoxysilane (PEG-Si, > 98%) and 11-aminoundecyltriethoxysilane (AUTES, > 97%) were purchased from Sikemia (Montpellier, France). Sodium chloride (NaCl) was obtained from VWR (Radnor, PA, USA). Cell Mask™ Orange Plasma Membrane was procured from Invitrogen (Cergy-Pontoise, France). Glass bottom 8-well tissue culture chambers were purchased from Sarstedt (Marnay, France).

C.2 Preparation of fluorophore-porphyrin (F-P) PMO NPs

Synthesis of P-Si by tetrasilylation of the commercial porphyrin (P)

Air was removed from porphyrin P (1.00 g, 1.48 mmol, 1.00 eq.) in a 100 mL two-neck round bottom flask. Then, anhydrous THF (14.8 mL, 182 mmol) and Et_3N (207 µL, 1.48 mol, 1.00 eq.) were added, followed by isocyanatopropyltriethoxysilane (1.54 mL, 6.24 mmol, 4.21 eq.). The reaction mixture was heated at 80 °C for 24 h. After resolubilization in ethyl acetate, the solvent was evaporated. Next, the crude product was washed on 0.22 µm polytetrafluoroethylene membrane with ethyl acetate and recrystallized in hexane using an ice bath. This step was repeated four times. After drying under vacuum, a purple powder was obtained (1.83 g, 74%). ^{1}H NMR (400 MHz, DMSO-d_6): δ=8.89 (s, 8H), 8.87 (s, 4H), 8.07 (d, *J*=8.5 Hz, 8H), 7.86 (d, *J*=8.5 Hz, 8H), 6.41 (t, 4H), 3.80 (q, *J*=7.0 Hz, 24H), 3.20 (m, 8H), 1.59 (m, 8H), 1.21 (t, *J*=7.0 Hz, 36H), 0.67 (m, 8H), -2.85 ppm (s, 2H). HRMS (ES^+, CH_3CN/CH_2Cl_2, 90/10): m/z calculated for $C_{84}H_{118}N_{12}O_{16}Si_4$: 1663.7944 $[M+H]^+$; found: 1663.79.

Synthesis of E-(4S)-F, E-(4S)-P and E-(4S)-F-P PMO NPs

A mixture of CTAB (250 mg, 0.69 mmol), ultrapure water (65 mL), and sodium hydroxide (NaOH (2 M), 437 µL) was stirred at 80 °C for 50 min at 750 rpm in a 250 mL round bottom flask. Then, a

mixture of 1,2-bis(triethoxysilyl)ethane, bis[3-(triethoxysilyl)propyl]tetrasulfide (E:4S, 100:0 or 80:20 (mol:mol), total=0.90 mmol), silylated fluorophore (F-Si, 7.5 mg, 4.5 µmol) and silylated porphyrin (P-Si, 67.4 mg, 40.5 µmol) in 5 mL of absolute ethanol was introduced in the reaction. The condensation process was conducted for 2 h. Then, the solution was cooled to room temperature while stirring; fractions were gathered in propylene tubes and collected by centrifugation for 20 min at 20,000 rpm. Subsequently, the surfactant-filled particles were solvent-extracted three times with ammonium nitrate solution (20 g L^{-1} ethanol) to remove the CTAB template, and washed three times with ethanol, water and ethanol. Each extraction and washing involved 20 min sonication at 40 °C and centrifugation for 15 min at 20,000 rpm. The NPs were finally redispersed in ethanol and dried for a few hours under vacuum at room temperature. Syntheses without fluorophore or porphyrin were also performed likewise. For the synthesis of E-(4S)-F PMO NPs, only 1 mL of absolute ethanol was used to prepare the sol-gel premix.

Synthesis of ENE-(4S)-F, ENE-(4S)-P and ENE-(4S)-F-P PMO NPs

A mixture of CTAB (50 mg, 0.14 mmol) and ultrapure water (30 mL) was stirred at 80 °C in a 100 mL round bottom flask until CTAB complete dissolution. Next, β-citronellol (19 µL, 105 µmol) and sodium hydroxide (NaOH (2 M), 160 µL) were added and the solution was stirred at 80°C for 30 min at 1000 rpm. Then, a mixture of 1,2-bis(triethoxysilyl)ethylene, bis[3-(triethoxysilyl)propyl]tetrasulfide (ENE:4S, 100:0 or 80:20 (mol:mol), total=0.65 mmol), silylated fluorophore (F-Si, 5.4 mg, 3.25 µmol) and silylated porphyrin (P-Si, 48.8 mg, 29.3 µmol) in 4 mL of absolute ethanol was introduced in the reaction. The condensation process was conducted for 2 h. Then, the solution was cooled to room temperature while stirring, and a purple precipitate was obtained after filtration with a Whatman® qualitative filter paper, Grade 6 (3 µm). The surfactants were extracted with a mixture of methanol (80 mL) and 36 wt% aqueous HCl solution (10 mL) for 24 h while stirring at 750 rpm. Fractions were gathered in propylene tubes and collected by centrifugation for 20 min at 20,000 rpm and washed 3 times with ethanol, water and ethanol. Each washing involved 20 min sonication at 40 °C and centrifugation for 15 min at 20,000 rpm. The NPs were finally redispersed in ethanol and dried for a few hours under vacuum at room temperature. Syntheses without fluorophore or without porphyrin were also performed likewise. For the synthesis of ENE-(4S)-F PMO NPs, only 0.8 mL of absolute ethanol was used to prepare the sol-gel premix.

Direct grafting of PEG-Si and AUTES on E-(4S)-F-P PMO NPs

After 2 h condensation process of E-(4S)-F-P PMO NPs, temperature was decreased to 50 °C. Then, a 25:1 (mol:mol) mixture of PEG-Si (80.7 mg, 196.5 µmol) and AUTES (2.6 mg, 7.9 µmol) was dissolved in 1 mL of ultrapure water and the resulting solution was added to the sol-gel preparation. The reaction was kept under stirring at 750 rpm and 50 °C overnight. Then, the reaction mixture was

cooled to room temperature while stirring. Half of the NPs was not treated with ammonium nitrate, and only redispersed in absolute ethanol and stored at +4 °C for further MAN grafting step. The other half was extracted and washed according to the previously described protocol for E-based NPs.

Direct grafting of PEG-Si and AUTES on ENE-(4S)-F-P PMO NPs

After 2 h condensation process of ENE-(4S)-F-P PMO NPs, temperature was decreased to 50 °C. Then, a 25:1 (mol:mol) mix of PEG-Si (60.1 mg, 146.2 µmol) and AUTES (2.0 mg, 5.8 µmol) was dissolved in 1 mL of ultrapure water and added to the sol-gel preparation. The reaction was kept under stirring at 750 rpm and 50 °C overnight. Then, the solution was cooled to room temperature while stirring, and a purple precipitate was obtained after filtration with a Whatman® qualitative filter paper, Grade 6 (3 µm). Half of the NPs was not treated with HCl and methanol, and only redispersed in absolute ethanol and stored at +4 °C for further MAN grafting step. The other half was extracted and washed according to the previously described protocol for ENE-based NPs.

Squarate mannose (MAN) derivative post-grafting using estimated AUTES amounts

The targeted AUTES:MAN ratio for post-grafting of MAN was 1:1 (mol:mol). Briefly, a mixture of F-P PMO@PEG NPs in EtOH (previously sonicated for 30 min without CTAB removal to avoid grafting in the pore walls) and MAN aqueous solution was stirred at 750 rpm and 50 °C overnight in a 50 mL round bottom flask (50:50 (v:v) H_2O:EtOH). The initial amount of mannose was ranging from 2 to 3 µg mg^{-1} F-P PMO@PEG NPs, depending on AUTES titration results. Then, ENE-based NPs filtration, CTAB extraction and NPs washings were performed according to the previously described protocols, depending on the type of NPs.

C.3 Photophysical studies of F-Si, P-Si and F-P PMO NPs

Photophysical properties were studied in EtOH and at room temperature (25 °C), using quartz cells of 1 cm path length.

Excitation and emission spectra of silylated chromophores

UV-visible absorption spectroscopy was performed with a Jasco V-770 spectrophotometer (Mary's Court Easton, MD, USA) on F-Si and P-Si dilute solutions (ca. 10^{-6} M in EtOH) to reach maximum absorbance $A_{max} \approx 0.1$. After that, steady-state fluorescence emission and excitation spectra were recorded on the Edinburgh Instruments FLS920 fluorimeter (Xe lamp) in photon-counting mode equipped with a dwell time of 0.1 s by exciting at $\lambda_{abs., max}$ (respectively 413 and 422 nm for F-Si and P-Si).

FRET efficiency of fluorophore-porphyrin PMO NPs

Energy transfer efficiency was evaluated by the fluorescence decrease of the energy donor (D = F) with the following equation:

$$\Phi_{ET} = 1 - \frac{I(DA)}{I(D)},$$

using either the fluorescence intensity of the donor, in the absence (I_D) and in the presence (I_{DA}) of the acceptor (A = porphyrin P) at the maximum emission wavelength of D, or the area under the corresponding fluorescence bands (results are the same in both cases). Emission spectra, recorded from a OPE at $\lambda_{exc.}$ = 413 nm, were measured on Jasco FP-8300 fluorimeter with identical PMO mass concentrations (44 µg mL^{-1} in EtOH). As F molar ratio in NPs is the same for all studied PMO (0.5% molar ratio), the number of absorbed photons at 413 nm by F was considered the same. Similarly, Two-Photon Excitation Fluorescence (TPEF) experiments were performed using a femtosecond laser chain (Ti-Sapphire Chameleon Ultra II, Coherent with pulse picker, generating 100-130 fs pulses at a 5 MHz rate) and an Ocean optics QEPro CCD detector with integration times ranging from 100 ms to 10 s. The excitation beam crossed a lens before arriving on the sample and a 750 nm short-pass filter after the sample to remove the excitation signal and prevent damages on the CCD detector. The beam power was measured with a PMD100 console and a S142C integrating sphere sensor from Thorlabs. Emission spectra (average of 10 measurements of 10 s integration time) of PMO NPs suspensions (44 µg mL^{-1} in EtOH) were recorded upon TPE at 850 nm.

C.4 Anticancer *in vitro* studies

Cell lines

MCF-7 human breast adenocarcinoma cells were maintained in Dulbecco's Modified Eagle's Medium (DMEM/F12) supplemented with 10% fetal bovine serum (FBS) and 1% penicillin/streptomycin. Cells were allowed to grow in humidified atmosphere at 37 °C under 5% CO_2.

MDA-MB-231 human breast adenocarcinoma cells were maintained in Dulbecco's Modified Eagle's Medium (DMEM/F12) supplemented with 10% FBS and 0.5% gentamycin. Cells were allowed to grow in humidified atmosphere at 37 °C under 5% CO_2.

OPE-PDT – MCF-7

MCF-7 cells were seeded in 96-well plates (Greiner Bio-One, Germany) at a density of 6000 cells *per* well. Cells were allowed to grow for 24 h, and then treated with NPs at 50 µg mL^{-1} for 24 h. Untreated cells were considered as a control. After incubation, cells were exposed (or not) to green light irradiation at 525 nm for 10 min duration (34 J cm^{-2}). The light beam was focused by a microscope objective lens (4×/0.10). Two days after irradiation, the percentage of cell viability was assessed using MTT assay.

Cell internalization study – MCF-7

MCF-7 cells were seeded in glass bottom 8-well tissue culture chambers (World Precision Instrument, Stevenage, UK) at sub-confluence. Twenty-four hours after seeding, cells were treated with 50 µg mL^{-1} of F-P PMO NPs for 24 h. Untreated cells were considered as a control. Fifteen minutes before the end of incubation, cells were treated with CellMask™ Orange (5 µg mL^{-1}, Invitrogen) for

membrane staining. Cells were washed two times with culture medium before observation with live confocal fluorescence microscope LSM780 (Carl Zeiss Microscope) equipped with a tunable femtosecond laser chain (Ti-Sapphire Chameleon Ultra II, Coherent with pulse picker, generating 140 fs wide pulses at 80 MHz rate) and excited at 561 nm for cell membranes and at 780 nm for NPs (TPEF), using for all a high magnification (63×/1.4 OIL DIC Plan-Apo).

TPE-PDT – MCF-7

MCF-7 cells were seeded in 384-well plates (Corning™ 4581) at a density of 2000 cells *per* well with 0.17 mm glass bottom in 50 µL of culture medium and allowed to grow for 24 h. Then, cells were incubated with or without 50 µg mL^{-1} of NPs for 24 h. Untreated cells were considered as a control. After incubation with NPs, cells were maintained in fresh culture medium, and then submitted (or not) to TPE with the LSM780 NLO microscope (Carl Zeiss Microscope). Half of the well was irradiated at 780 nm by three scans of 1.26 s duration in four different areas of the well with a focused laser at a maximum laser power, not to irradiate overlapping areas. The laser beam was focused by a microscope objective lens (Carl Zeiss 10×/0.3 EC Plan-Neofluar) at maximum laser power (3 W input, 900 mW cm^{-2} output before the objective). The scan size does not allow irradiating more areas without overlapping. Wells were then incubated for 48 h. Fifteen minutes before the end of incubation, cells were treated with Hoechst 33342™ at a final concentration of 2.5 µg mL^{-1} for a nuclear labelling of living cells. Observation with fluorescence microscope Evos™ M5000 Imaging System (Thermo Fisher Scientific, France) equipped with DAPI filter using 4× magnification gave values for living cells quantification after processing a counting method. This method can be reproduced on all images of a batch in an identical way and served to count the nuclei and to establish a percentage of cell viability according to the following equation:

$$\frac{Number\ of\ nuclei\ in\ the\ well}{Number\ of\ nuclei\ in\ the\ control\ well} \times 100,$$

then, the viability was corrected according to the following formula:

(non-irradiated viability – 2 × (non-irradiated viability – irradiated viability)).

Data are mean values standard deviation from six or eight independent experiments (three or four wells by two counting methods on Evos™ M5000).

2.5 Anticancer *in vivo* studies

Cell culture. Human breast cancer cells stably expressing red fluorescent protein **(**MDA-MB-231-Luc-RFP) were purchased from AMSBIO (SC041, Abingdon, UK) and maintained in Dulbecco's Modified Eagle Medium (DMEM) supplemented with 10% FBS and 5 µg mL^{-1} blasticidin as a selection antibiotic. **Zebrafish breeding conditions.** Casper zebrafish embryos were purchased from Zebrafish International Resource Center (ZIRC) as embryos and housed in the ZeNeuro platform (Inserm U1198, Montpellier University) under conditions previously described by some of us.[42] Experiments with zebrafish embryos

until 96 h post fertilization (hpf) are considered as *in vitro* studies according to the EU Directive 2010/63/EU on the protection of animals used for scientific purposes.[42]

TPE-PDT study in zebrafish embryos. MDA-MB-231-Luc-RFP cells were seeded in Nunc™ EasYFlask™ 75 cm^2. Twenty-four hours after seeding, cells were treated or not with 50 µg mL^{-1} of ENE-4S-F-P@MAN for 24 h. After incubation, the cells were washed twice with PBS, trypsinized and collected in culture medium. After counting, the cells were centrifuged at 1300 rpm for 5 min at 4 °C, then suspended in the required volume of PBS containing 2% FBS to have a solution of 3×10^7 cells *per* 1 mL. The cell solution was kept on ice until injection. Casper embryos at 30 hpf were used after dechorionation. The embryos were anesthetized with tricaine solution (168 mg mL^{-1}) for 10 min prior to injection. Then, the embryos were placed on an agar mold for the microinjection of cells previously incubated (or not) with NPs. Each embryo received 1-2 pulses of 5 nL of cell suspension in the yolk. Injected Casper embryos with cells without any treatment with NPs were used as the control. After injection, embryos were placed in E3 medium and kept at 31 °C. Twenty-four hours after injection, the embryos were anesthetized and imaged using confocal microscopy LSM780 and objective 10×/0.3 EC Plan-Neofluar at 561 nm excitation to visualize the xenograft in red colour (T0). After imaging, the embryos with xenograft of cells alone (control) or cells previously treated with NPs (ENE-4S-F-P@MAN) were divided into two groups: no laser irradiation and laser irradiation at 780 nm. Each embryo in the laser irradiation group was exposed to six scans of 1.26 s duration using confocal microscopy LSM780 NLO equipped with multiphoton source (Chameleon Ultra-II Coherent laser) and objective 10×/0.3 EC Plan-Neofluar (0.3 numerical aperture). Twenty-four hours after irradiation, the embryos were imaged again (T24). The fluorescence intensity of the xenograft before and after irradiation was quantified using ImageJ program. The corrected total cell fluorescence (CTCF) was calculated as CTCF = Integrated Density – (Area of selected cell × Mean fluorescence of background readings) and the tumor regression (%) was calculated by considering the fluorescence intensity value of each embryo before irradiation is 100%.

Statistical analysis.

Data are presented as the mean ± standard deviation. Statistical analysis was performed using GraphPad Prism. The comparison between groups was analyzed with Student's t test. Differences between irradiated and non-irradiated samples were considered statistically significant when p values were less than 0.05 (*p <0.05).

CONCLUSIONS

Organosilica NPs with small and well-defined mesopores were prepared by simple routes using different combinations of organoalkoxysilane precursors. The NPs were characterized by several

techniques and showed morphology, chemical structure and particle size that are suitable for biological applications.

We confirmed that the PMO NPs, integrating trisilylated octupolar fluorophore moieties, possess high two-photon absorption cross-sections in the near-infrared region as well as tetrasilylated porphyrin PS moieties within their hybrid framework. Fluorescence measurements demonstrated efficient intraparticle FRET from the two-photon energy donors to the porphyrin energy acceptors.

Different surface functionalization strategies were attempted for further modifying these photoactive NPs to provide a range of samples with different functionalities. All of them (either pristine, bearing short-length PEG or a PEG/mannose combination) presented significant levels of cellular uptake in MCF-7 and MDA-MB-231 cancer cells that were evaluated from the intrinsic fluorescence of the NPs upon 780 nm TPE. In addition, high TPE-PDT efficiency was obtained against MCF-7 cancer cells *in vitro*. Subsequent TPE-PDT studies on biodegradable ENE-4S-F-P NPs incubated with MDA-MB-231 breast cancer cells suggested the targeting specificity of mannose phenyl squarate for a reduced incubation time.

Finally, zebrafish embryos were used as *in vivo* models to assess the therapeutic potential of mannose-grafted ENE-4S-F-P PMO NPs. A decrease in RFP level is correlated with living cancer cells decrease, and this was observed in the group of embryos injected with cancer cells beforehand incubated with two-photon active nanoplatforms, and then submitted to TPE-PDT.

Altogether, the design strategies that were developed with these mixed PMO NPs allowed obtaining suitable materials for anticancer TPE-PDT which hold great promises for combination therapy using the two-photon active organosilica framework alongside with nanoparticle porosity for drug delivery.

Author contributions

Clarence Charnay, Jean-Olivier Durand, Nicolas Bondon, Sabine Szunerits, Nadir Bettache, Magali Gary-Bobo, Olivier Mongin and Christophe Nguyen designed research.

Nicolas Bondon, Clément Charlot, Alexandre Barras, Jean-Olivier Durand, Lamiaa M. A. Alii, Denis Durand, Christophe Nguyen, Nadir Bettache, Erwan Oliviero, Nicolas Richy, Grégory Taupier and Yann Molard conducted research.

Nicolas Bondon, Christophe Nguyen and Lamiaa M.A. Alii wrote the paper.

Christophe Nguyen, Lamiaa M.A. Alii, Magali Gary-Bobo, Rabah Boukherroub, Alexandre Barras, Sabine Szunerits, Frédéric Paul, Jean-Olivier Durand, Nicolas Bondon and Clarence Charnay performed review and editing.

Clarence Charnay, Jean-Olivier Durand and Magali Gary-Bobo performed supervision; project administration was done by Clarence Charnay.

Funding acquisition was done by Olivier Mongin, Jean-Olivier Durand, Nadir Bettache, Rabah Boukherroub and Clarence Charnay. Clarence Charnay had primary responsibility for the final content. The manuscript was written through contributions of all authors.

Conflicts of interest

The authors declare no competing financial interest.

Data availability

Acknowledgments

This work was supported by the Agence Nationale de la Recherche: ANR-19-CE09-0034 (MSN-2hv).

Notes and references

1 S. Mallidi, S. Anbil, A. L. Bulin, G. Obaid, M. Ichikawa and T. Hasan, *Theranostics*, 2016, **6**, 2458–2487.

2 J. Zhao, D. Zhong and S. Zhou, *J. Mater. Chem. B*, 2018, **6**, 349–365.

3 A. Vangara, A. Pramanik, Y. Gao, K. Gates, S. Begum and P. C. Ray, *ACS Appl. Bio Mater.*, 2018, **1**, 298–309.

4 F. Bolze, S. Jenni, A. Sour and V. Heitz, *Chem. Commun.*, 2017, **53**, 12857–12877.

5 Z. Sun, L. P. Zhang, F. Wu and Y. Zhao, *Adv. Funct. Mater.*, 2017, **27**, 1704079.

6 A. Soleimany, S. Khoee, D. Dastan, Z. Shi, S. Yu and B. Sarmento, *J. Photochem. Photobiol. B*, 2023, **238**, 112602.

7 X. Gan, H. Wang, L. Lu, H. Li, K. Wang, L. Kong, F. Li, Y. Tian, J. Wu and H. Zhou, *Dye Pigment.*, 2018, **150**, 27–35.

8 L. Shi, C. Nguyen, M. Daurat, N. Richy, C. Gauthier, E. Rebecq, M. Gary-Bobo, S. Cammas-Marion, O. Mongin, C. O. Paul-Roth and F. Paul, *Cancers (Basel).*, 2022, **14**, 2358.

9 Y. Shen, A. J. Shuhendler, D. Ye, J. J. Xu and H. Y. Chen, *Chem. Soc. Rev.*, 2016, **45**, 6725–6741.

10 A. P. Sherje, M. Jadhav, B. R. Dravyakar and D. Kadam, *Int. J. Pharm.*, 2018, **548**, 707–720.

11 K. McNamara and S. A. M. Tofail, *Adv. Phys. X*, 2017, **2**, 54–88.

12 W. T. Al-Jamal and K. Kostarelos, *Nanomedicine*, 2007, **2**, 85–98.

13 A. M. Caminade, A. Zibarov, E. C. Diaz, A. Hameau, M. Klausen, K. M. C. Ching, J. P. Majoral, J. B. Verlhac, O. Mongin and M. Blanchard-Desce, *Beilstein J. Org. Chem.*, 2019, **15**, 2287–2303.

14 S. S. Lucky, K. C. Soo and Y. Zhang, *Chem. Rev.*, 2015, **115**, 1990–2042.

15 Y. P. Chen, L. Xu, T. W. Tang, C. H. Chen, Q. H. Zheng, T. P. Liu, C. Y. Mou, C. H. Wu and S. H. Wu, *ACS Appl. Mater. Interfaces*, 2020, **12**, 56741–56752.

16 T. I. Hsu, Y. P. Chen, R. L. Zhang, Z. A. Chen, C. H. Wu, W. C. Chang, C. Y. Mou, H. W. H. Chan and S. H. Wu,

ACS Appl. Mater. Interfaces, 2024, **16**, 21722–21735.

17 N. Prabhakar, E. Långbacka, E. Özliseli, J. Mattsson, A. Mahran, I. Suleymanova, C. Sahlgren, J. M. Rosenholm, M. Åkerfelt and M. Nees, *Small Sci.*, 2024, **2400084**, 1–12.

18 N. Alvarez and A. Sevilla, *Int. J. Mol. Sci.*, 2024, **25**, 1023.

19 Y. Huang, F. Qiu, R. Chen, D. Yan and X. Zhu, *J. Mater. Chem. B*, 2020, **8**, 3772–3788.

20 P. Fathi and Di. Pan, *Nanomedicine*, 2020, **15**, 2493–2515.

21 J. Wang, Y. Zhong, X. Wang, W. Yang, F. Bai, B. Zhang, L. Alarid, K. Bian and H. Fan, *Nano Lett.*, 2017, **17**, 6916–6921.

22 S. Kim, T. Y. Ohulchanskyy, H. E. Pudavar, R. K. Pandey and P. N. Prasad, *J. Am. Chem. Soc.*, 2007, **129**, 2669–2675.

23 R. S. Guimarães, C. F. Rodrigues, A. F. Moreira and I. J. Correia, *Pharmacol. Res.*, 2020, **155**, 104742.

24 Y. Cheng, X. Jiao, W. Fan, Z. Yang, Y. Wen and X. Chen, *Biomaterials*, 2020, **256**, 120191.

25 X. Du, F. Kleitz, X. Li, H. Huang, X. Zhang and S. Z. Qiao, *Adv. Funct. Mater.*, 2018, **28**, 1707325.

26 X. Du, X. Li, L. Xiong, X. Zhang, F. Kleitz and S. Z. Qiao, *Biomaterials*, 2016, **91**, 90–127.

27 Y. Chen and J. Shi, *Adv. Mater.*, 2016, **28**, 3235–3272.

28 J. G. Croissant, X. Cattoën, M. WongChi Man, J. O. Durand and N. M. Khashab, *Nanoscale*, 2015, **7**, 20318–20334.

29 N. X. D. Mai, T. H. T. Nguyen, L. B. Vong, M. H. D. Dang, T. T. T. Nguyen, L. H. T. Nguyen, H. K. T. Ta, T. H. Nguyen, T. B. Phan and T. L. H. Doan, *Mater. Sci. Eng. C*, 2021, **127**, 112232.

30 S. Chinnathambi and F. Tamanoi, *Pharmaceutics*, 2020, **12**, 1–15.

31 Z. Teng, W. Li, Y. Tang, A. Elzatahry, G. Lu and D. Zhao, *Adv. Mater.*, 2019, **31**, 1–24.

32 C. Xu, C. Lei, Y. Wang and C. Yu, *Angew. Chemie - Int. Ed.*, 2022, **61**, e202112752.

33 S. Yang, J. Fan, S. Lin, Y. Wang and C. Liu, *Colloids Surf. A*, 2020, **585**, 124133.

34 J. Chen, Y. Wang, B. Ma, L. Guan, Z. Tian, K. Lin and Y. Zhu, *Appl. Mater. Today*, 2020, **19**, 100655.

35 P. Picchetti, B. N. DiMarco, L. Travaglini, Y. Zhang, M. C. Ortega-Liebana and L. De Cola, *Chem. Mater.*, 2020, **32**, 392–399.

36 T. Doura, T. Nishio, F. Tamanoi and M. Nakamura, *J. Mater. Res.*, 2019, **34**, 1266–1278.

37 N. Bondon, N. Richy, L. M. A. Ali, D. Durand, M. Gary-Bobo, Y. Molard, G. Taupier, F. Paul, N. Bettache, J. O. Durand, C. Nguyen, C. Charnay and O. Mongin, *Tetrahedron*, 2023, **144**, 133577.

38 N. S. Makarov, M. Drobizhev and A. Rebane, *Opt. Express*, 2008, **16**, 4029.

39 D. Aggad, C. M. Jimenez, S. Dib, J. G. Croissant, L. Lichon, D. Laurencin, S. Richeter, M. Maynadier, S. K. Alsaiari, M. Boufatit, L. Raehm, M. Garcia, N. M. Khashab, M. Gary-Bobo and J. O. Durand, *ChemNanoMat*, 2018, **4**, 46–51.

40 B. Mezghrani, L. M. A. Ali, S. Richeter, J. O. Durand, P. Hesemann and N. Bettache, *ACS Appl. Mater. Interfaces*, 2021, **13**, 29325–29339.

41 B. Mezghrani, L. M. A. Ali, S. Jakimoska, F. Cunin, P. Hesemann, J. O. Durand and N. Bettache, *Chempluschem*, 2023, **88**, e202300021.

42 B. Mezghrani, L. M. A. Ali, N. Cubedo, M. Rossel, P. Hesemann, J. O. Durand and N. Bettache, *Int. J.*

Pharm., 2023, **641**, 123083.

43 S. Biswas, H. Ahn, M. V Bondar and K. D. Belfield, *Langmuir*, 2012, **2**, 1515–1522.

44 C. Mauriello Jimenez, D. Aggad, J. G. Croissant, K. Tresfield, D. Laurencin, D. Berthomieu, N. Cubedo, M. Rossel, S. Alsaiari, D. H. Anjum, R. Sougrat, M. A. Roldan-Gutierrez, S. Richeter, E. Oliviero, L. Raehm, C. Charnay, X. Cattoën, S. Clément, M. Wong Chi Man, M. Maynadier, V. Chaleix, V. Sol, M. Garcia, M. Gary-Bobo, N. M. Khashab, N. Bettache and J. O. Durand, *Adv. Funct. Mater.*, 2018, **28**, 1800235.

45 Q. Wu, R. Xia, C. Li, Y. Li, T. Sun, Z. Xie and X. Jing, *Mater. Chem. Front.*, 2021, **5**, 8333–8340.

46 B. Guan, Y. Cui, Z. Ren, Z. A. Qiao, L. Wang, Y. Liu and Q. Huo, *Nanoscale*, 2012, **4**, 6588–6596.

47 Y. Song, D. Cheng, J. Luo, M. Zhang and Y. Yang, *J. Colloid Interface Sci.*, 2021, **591**, 129–138.

48 V. Agarwal, M. Singh, G. McPherson, V. John and A. Bose, *Colloids Surf. A*, 2006, **281**, 246–253.

49 Y. Li, L. Bi, S. Wang, Y. Chen, B. Li, X. Zhu and Y. Yang, *Chem. Commun.*, 2010, **46**, 2680–2682.

50 J. Croissant, X. Cattoën, M. Wong Chi Man, A. Gallud, L. Raehm, P. Trens, M. Maynadier and J. O. Durand, *Adv. Mater.*, 2014, **26**, 6174–6180.

51 Z. Zhou, R. N. K. Taylor, S. Kullmann, H. Bao and M. Hartmann, *Adv. Mater.*, 2011, **23**, 2627–2632.

52 S. Brunauer, P. H. Emmett and E. Teller, *J. Am.Chem.Soc.*, 1938, **60**, 309–319.

53 Y. Ding, Y. Dai, M. Wu and L. Li, *Chem. Eng. J.*, 2021, **426**, 128880.

54 J. Sturge, D. Wienke, L. East, G. E. Jones and C. M. Isacke, *J. Cell Biol.*, 2003, **162**, 789–794.

55 D. Brevet, M. Gary-Bobo, L. Raehm, S. Richeter, O. Hocine, K. Amro, B. Loock, P. Couleaud, C. Frochot, A. Morère, P. Maillard, M. Garcia and J. O. Durand, *Chem. Commun.*, 2009, 1475–1477.

56 A. Akbari, R. Yegani and B. Pourabbas, *Colloids Surf. A*, 2015, **484**, 206–215.

57 Y. Qie, H. Yuan, C. A. Von Roemeling, Y. Chen, X. Liu, K. D. Shih, J. A. Knight, H. W. Tun, R. E. Wharen, W. Jiang and B. Y. S. Kim, *Sci. Rep.*, 2016, **6**, 1–11.

58 O. K. Nag and V. Awasthi, *Pharmaceutics*, 2013, **5**, 542–569.

59 S. Udenfriend, S. Stein, P. Böhlen, W. Dairman, W. Leimgruber and M. Weigele, *Science*, 1972, **178**, 871–872.

60 J. Motoyoshiya, S. Tomioka, D. Kobayashi and T. Fujimoto, *Tetrahedron Lett.*, 2018, **59**, 1104–1107.

61 J. Croissant, M. Maynadier, A. Gallud, H. Peindy N'Dongo, J. L. Nyalosaso, G. Derrien, C. Charnay, J. O. Durand, L. Raehm, F. Serein-Spirau, N. Cheminet, T. Jarrosson, O. Mongin, M. Blanchard-Desce, M. Gary-Bobo, M. Garcia, J. Lu, F. Tamanoi, D. Tarn, T. M. Guardado-Alvarez and J. I. Zink, *Angew. Chemie - Int. Ed.*, 2013, **52**, 13813–13817.

62 S. H. Cheng, C. C. Hsieh, N. T. Chen, C. H. Chu, C. M. Huang, P. T. Chou, F. G. Tseng, C. S. Yang, C. Y. Mou and L. W. Lo, *Nano Today*, 2011, **6**, 552–563.

63 B. Valeur and M. N. Berberan-Santos, *Molecular Fluorescence: Principles and Applications*, Wiley, 2012.

64 S. Zhao, J. Huang and J. Ye, *J. Exp. Clin. Cancer Res.*, 2015, **34**, 1–9.

65 O. Sperling, A. Fuchs and T. K. Lindhorst, *Org. Biomol. Chem.*, 2006, **4**, 3913–3922.